remote sensing

MDPI

Communication

Design and Implementation of K-Band Electromagnetic Wave Rain Gauge System

Jeongho Choi [1] and Sanghun Lim [2,*]

[1] Hyper-Converged Forensic Research Center for Infrastructure, Korea University, Anam-ro 145, Seongbuk-gu, Seoul 02841, Republic of Korea; jcspatium@gmail.com
[2] Korea Institute of Civil Engineering and Building Technology, Goyang-daero, Ilsanseo-gu, Goyang-si 10223, Republic of Korea
* Correspondence: slim@kict.re.kr

Abstract: In order to prevent and manage damage caused by localized torrential downpours, the quantitative observation of rainfall is crucial. Considering the spatial complexity and vertical variability of rainfall, it is important to obtain low-altitude, high-resolution radar observations to reduce uncertainty in radar rainfall estimates. In this paper, we present an electromagnetic wave rainfall gauge system (EWRG) that detects rainfall within the observation area and estimates the areal rainfall using electromagnetic waves. The EWRG system was developed based on a subminiature size antenna, a K-band dual-polarization transceiver, and advanced high-resolution, high-speed signal processing technology. The system design and signal processing techniques are described in detail. The EWRG has the advantage of overcoming the limitations of conventional cylindrical ground rain gauges, such as the contamination and spatial inaccuracy of rain gauges, which cause uncertainty in quantitative precipitation measurement.

Keywords: electromagnetic wave rain gauge; K-band; dual polarization; antenna; transceiver; signal processing

Citation: Choi, J.; Lim, S. Design and Implementation of K-Band Electromagnetic Wave Rain Gauge System. *Remote Sens.* **2024**, *16*, 6. https://doi.org/10.3390/rs16010006

Academic Editor: Silas Michaelides

Received: 11 October 2023
Revised: 7 December 2023
Accepted: 11 December 2023
Published: 19 December 2023

1. Introduction

Due to climate change, the localized characteristics of heavy rainfall have increased, and the irregularities in rainfall distribution have intensified. Consequently, there are limitations in applying traditional flood forecasts, which assume uniform rainfall distribution over one representative area, to the current altered meteorological environment [1,2]. The ground rain gauge, commonly used for rainfall observations, has a diameter of 20 cm (area of 0.04 m^2). However, the representative area covered by one rain gauge used in flood forecast models can span from tens to hundreds of square kilometers. Nevertheless, the spatial variability in rainfall within this representative area is significant, leading to increased uncertainty in flood forecasts and reduced usability. Furthermore, conventional rain gauges inherently encompass systemic errors stemming from various factors such as dryness, evaporation, wind, errors in tipping buckets, and poor maintenance, leading to errors in rainfall observations themselves [3,4]. This has also been a cause for the decrease in accuracy during ground correction for meteorological radars for data assimilation. Consequently, there have been recent efforts to develop and distribute equipment (such as Parsivel, disdrometers, POSS, etc.) to replace conventional rain gauges. However, these devices still face challenges in measuring spatial distributions effectively, and thus have not provided a solution to the issue of representativeness. Conversely, weather radars are utilized for detecting precipitation spatial distributions over wide ranges [5]. Flood forecasting technologies based on radars have also been significantly developed. However, they are primarily installed at high altitudes like mountain peaks, avoiding ground obstacles, especially in Korea. This leads to significant discrepancies with ground rainfall, and during the process of estimating rainfall through calibration with traditional ground rain

gauges, errors can still occur [6]. Thus, there are still limitations in accurately forecasting floods and observing localized heavy rainfall. In this context, it is evident that for effective flood forecasting, which is crucial for disaster prevention, a technology capable of accurately measuring the spatial distribution of ground precipitation amounts is needed. This technology should be able to measure ground rainfall without being affected by terrain features like flatlands and mountainous areas, similar to conventional cylindrical ground rain gauges. It should perform the same function as traditional rain gauges in observing actual rainfall, while overcoming the shortcomings of existing technology. Additionally, a new rainfall measuring instrument that can densely measure actual rainfall distribution in high-density areas like urban ones should be developed, enabling the utilization of this technology for preventing localized disasters such as torrential heavy rainfall, urban flooding, and landslides.

With this perspective in mind, this study has developed precipitation observation equipment based on electromagnetic waves, providing a high-resolution spatial distribution of ground rainfall. This equipment accurately measures localized heavy rainfall, with the aim of mitigating damages caused by such events and preventing disasters like flooding and landslides. This paper describes the high-resolution electromagnetic wave rain gauge, referred to as the 'EWRG', capable of measuring both rainfall and wind fields [7]. Note that the micro-rain radar (MRR) can serve as an alternative method for estimating rainfall using electromagnetic waves [8]. The MRR operates as a vertical pointing frequency-modulated continuous wave (FMCW) system, whereas the EWRG functions as a scanning dual-polarization system. The EWRG has been developed by integrating advanced technologies, encompassing ultra-compact dual-polarization antenna technology, K-band dual-polarization transceiver technology, high-resolution high-speed signal processing technology, and low-loss radome technology.

This paper is organized as follows. The system design and implementation of EWRG is described in Section 2. The proposed signal processing method of the EWRG and preliminary results of evaluation are discussed in Section 3. Finally, the summary and conclusion are presented in Section 4.

2. EWRG System Design and Implementation

The EWRG is a K-band electromagnetic wave-based rain gauge system [9]. The hardware consists of an antenna, a transceiver that transmits and receives electromagnetic signals, and a signal processor that converts received signals into observation variables of the EWRG. The software is composed of an operation control software responsible for operating and controlling both hardware and software, a data processing module handling data quality management and rainfall estimation, and a control/display GUI program performing remote control and data visualization of the system. Figure 1 and Table 1 illustrate the system diagram and major specifications of the EWRG.

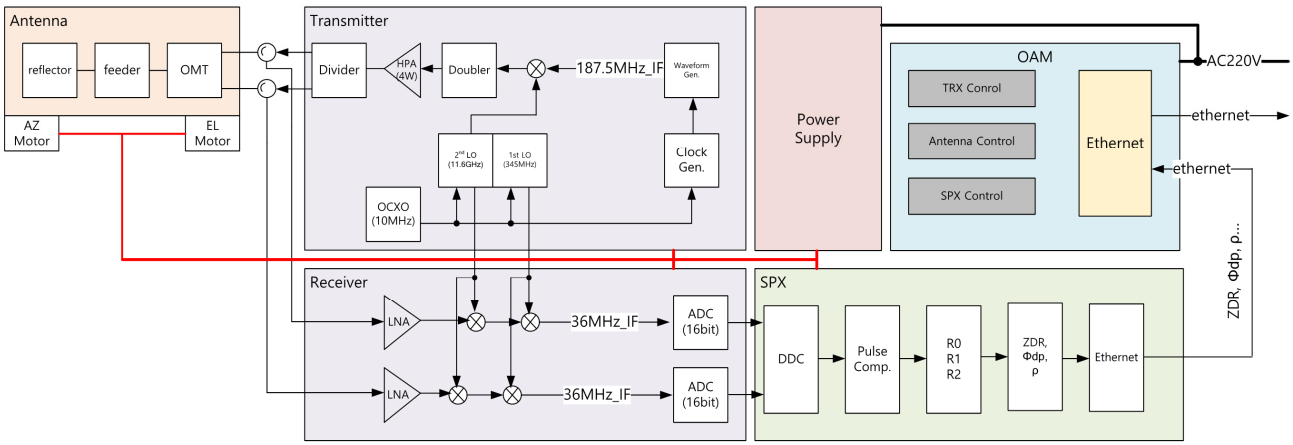

Figure 1. EWRG system diagram.

Table 1. Specifications of EWRG.

	Specification
Operating frequency (GHz)	24.15
Transmission power (W)	4 (horizontal/vertical)
Polarization	Simultaneous dual polarization (H/V)
Antenna shape	Parabolic reflector type
Antenna diameter (cm)	50 (carbon)
Beam width (deg.)	1.6 (H/V)
Gain (dBi)	above 40
Driving range (deg.)	Azimuth: 0~360; Elevation: −2~+92
Driving speed (RPM)	Azimuth: 6; Elevation: 2
Signal form	I/Q demodulation
Effective observation range (m)	150~3000
Waveform	LFM Pulse
Pulse width (μs)	0.2, 1
PRF (KHz)	10
Distance resolution (m)	30
Minimum Detectable Signal (dBm)	−90
ADC resolution (bit)	14

2.1. Transceiver

The transceiver performs the transmission function by up-converting and amplifying the LFM (Linear Frequency Modulation) signal generated from the waveform generator, and then sends out the resulting high-power K-band signal through the antenna. It also performs the reception function, which includes amplifying the received K-band signal from the antenna, down-converting it, and then sending it to the signal processor. In this paper, we developed a K-band pulse-driven 4 W Solid State Power Amplifiers (SSPA) transceiver using a small Hybrid Microwave Integrated Circuit (HMIC) [10–12]. The transceiver comprises a power supply, a transmitter, and a receiver. It delivers over 4 W of output power and maintains a receiving Noise Figure (NF) of less than 5 dB with a short duty cycle of 1% even in high-temperature environments of up to 65 degrees. Figure 2 displays the developed transceiver.

Figure 2. The EWRG transceiver.

2.1.1. LFM Waveform

The EWRG transceiver employs the LFM method for signal transmission [13]. The LFM signal can be either a triangular wave, which linearly increases or decreases over time, or a sawtooth wave, which starts with a linear increase and then returns to the base frequency. The time difference between the transmitted and received signals varies with distance [14]. By accumulating distance information during the Coherent Pulse Interval (CPI) and subsequently performing Fast Fourier Transform (FFT) processing, speed information can be extracted. Figure 3 depicts the concept diagram of LFM signal transmission and reception. In Figure 3, the red line represents the transmission signal modulated with a linear frequency, while the yellow and blue lines represent the received signals returned from two objects. Δt represents the time difference between transmission and reception, providing information about the distance between the object and the radar. Δf indicates the frequency difference between the transmission and reception signals, which corresponds to the Doppler frequency and relative speed compared to the object [15].

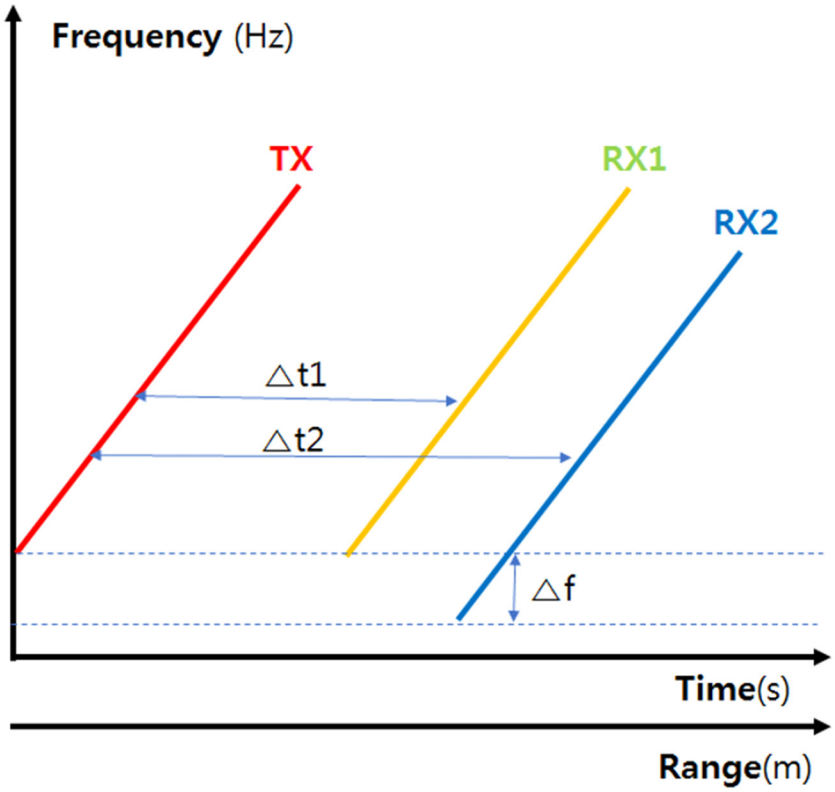

Figure 3. LFM transmission and reception concept diagram. TX: transmitted signal, RX: received signal.

The LFM signal, expressed as θ(t), can be implemented by linearly modulating the frequency over time and can be expressed as Equation (1). If the time variable 't' is replaced by the number of loop repetitions (i) and the time interval (Δt), it can be expressed as Equation (2). Here, f_c represents the center frequency, f_{start} is the frequency where modulation begins, f_{stop} is the frequency where modulation ends, and T signifies the period [16–18].

$$\theta(t) = 2\pi\left(f_c t + \frac{f_{start} - f_{stop}}{2T} t^2\right) \quad (1)$$

$$\theta(t) = 2\pi\left(f_c(i \times \Delta t) + \frac{f_{start} - f_{stop}}{2(\text{sample No.} * \Delta t)} (i * \Delta t)^2\right) \quad (2)$$

2.1.2. Transmitter

The transmitter is responsible for up-converting the Intermediate Frequency (IF) band CHIRP signal generated by the waveform generator to the K band. It then amplifies the signal to over 4 W using a high-power amplifier (HPA) and delivers it to antennas along both the vertical and horizontal paths. Figure 4 depicts the block diagram of the transmitter [19].

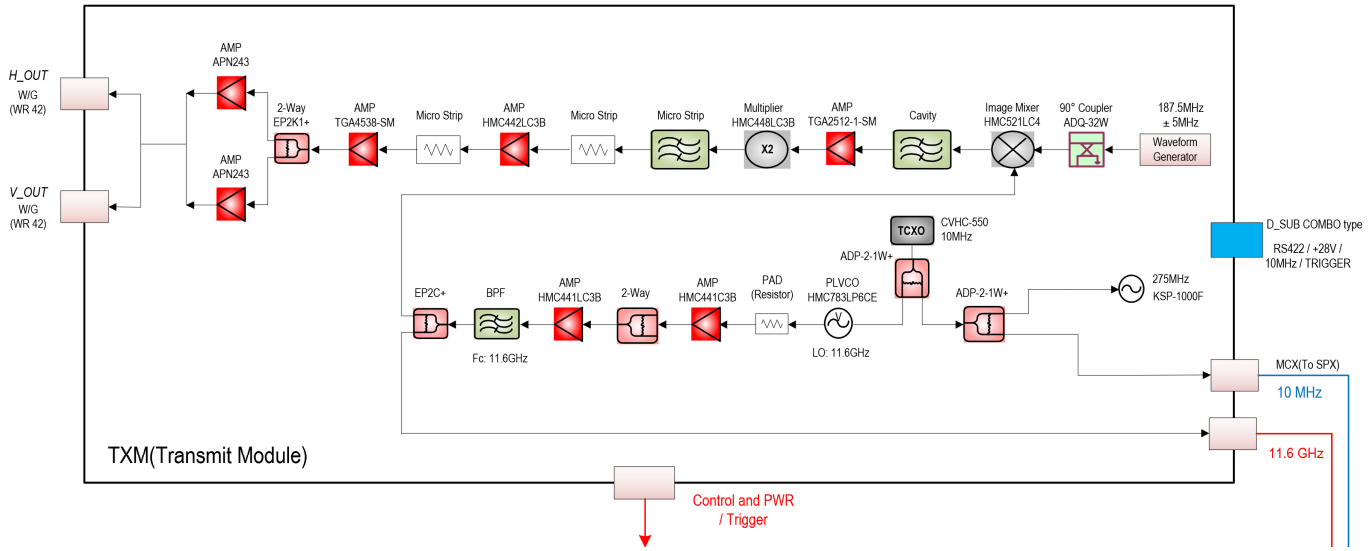

Figure 4. Block diagram of EWRG transmitter.

The waveform generator utilizes a precision Direct Digital Synthesizer (DDS) chip to generate CHIRP waveforms (5 MHz bandwidth) in the IF frequency band (187.15 MHz). The waveform generator is designed as a separate Printed Circuit Board (PCB) assembly in the transmitter module. Figure 5 shows LFM wave form at a horizontal and vertical port. In the bottom-left images of Figure 5a,b, we can observe a linear increase in frequency [20].

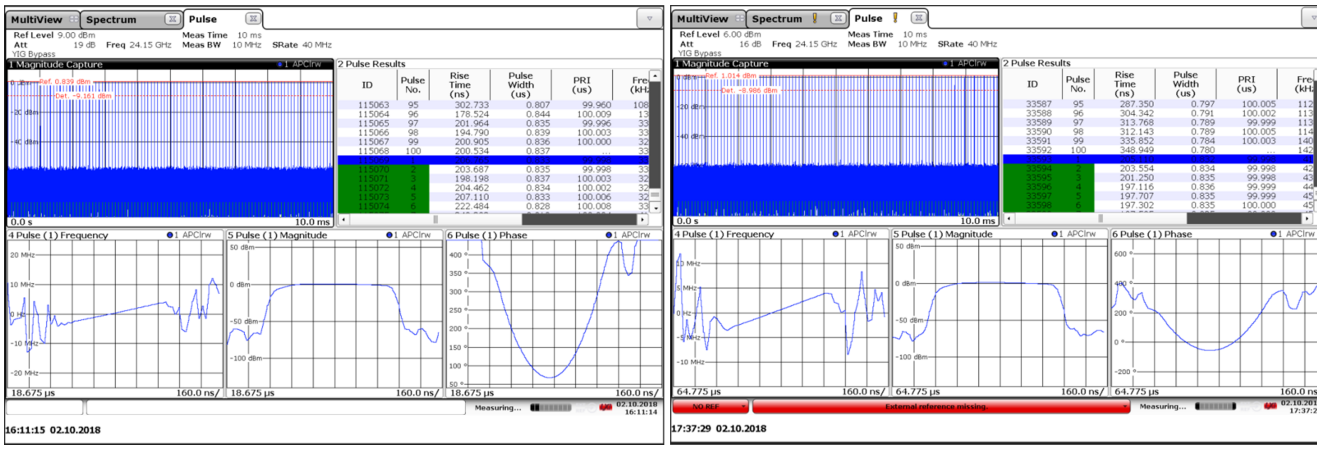

(**a**) (**b**)

Figure 5. LFM waveform (**a**) at horizontal and (**b**) at vertical port.

The power budget and the frequency stability of the transmitter are shown in Figures 6 and 7, respectively.

2.1.3. Receiver

The receiver amplifies the received horizontal and vertical K-band signals with a Low Noise Amplifier (LNA), and then converts them into IF signals through Double Conversion.

It subsequently forwards these processed signals to the signal processor. Figure 8 depicts the block diagram of the transmitter. Figure 9 indicates the power budget of the receiver.

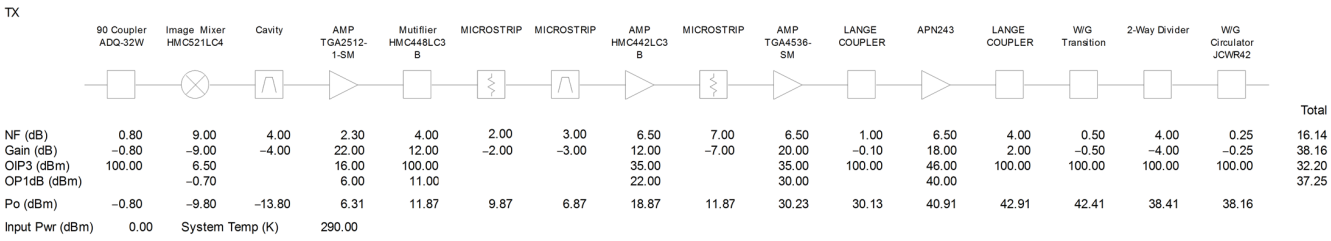

Figure 6. The power budget of the transmitter.

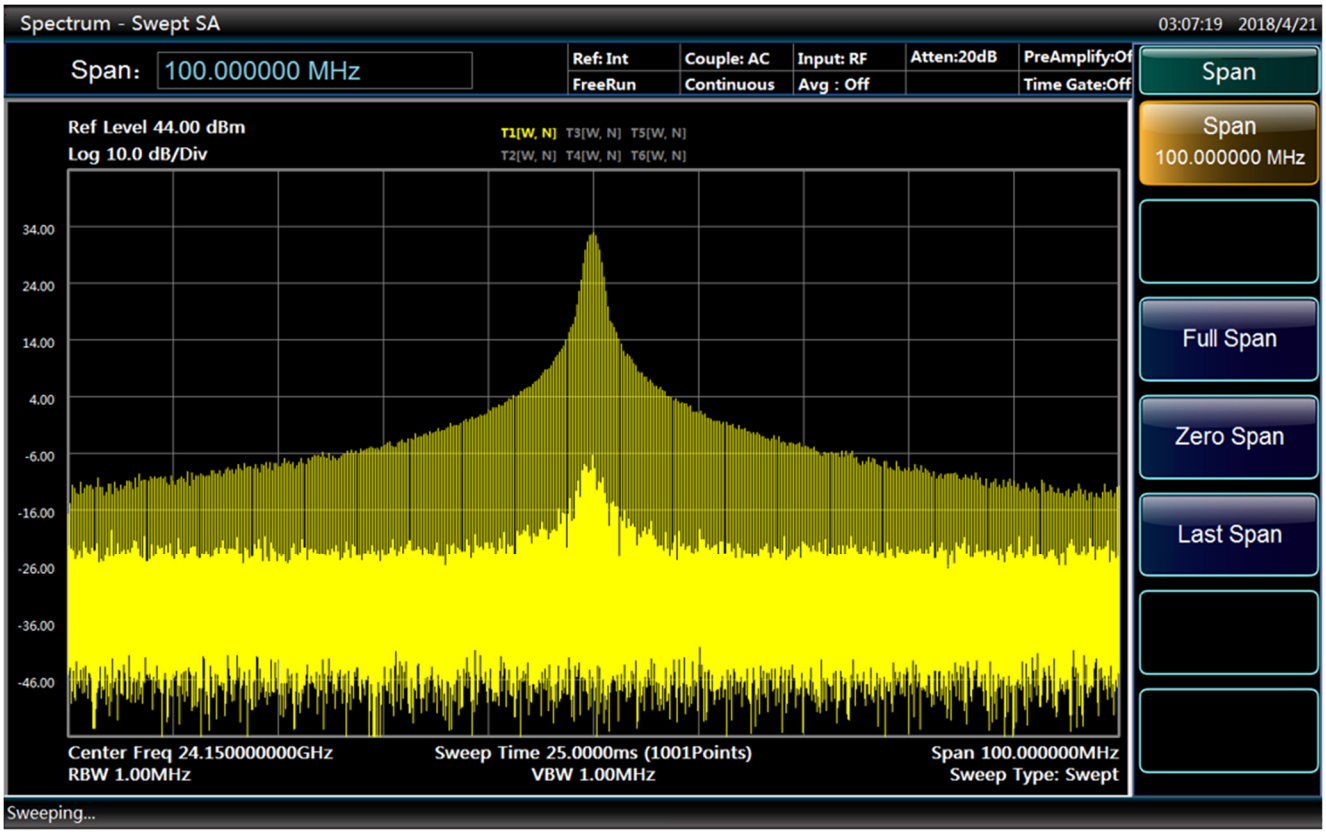

Figure 7. Frequency stability of the transmitter.

2.2. Antenna and Radome

The antenna module consists of an antenna unit, a driving unit, and an antenna control unit (ACU). Figure 10a,b depict the 3D design and block diagram of the antenna, respectively. The antenna unit is responsible for simultaneously transmitting and receiving horizontal and vertical signals. It is primarily composed of a 50 cm diameter carbon reflector, a feedhorn, and an Orthomode Transducer (OMT). The driving unit is designed with a two-axis structure for driving in the azimuth or elevation directions, and a reducer-integrated motor is used to drive each axis. The ACU controls motors to move the antenna in azimuth or elevation directions and interfaces with external devices. In this project, the EWRG adopted a slip ring to prevent the twisting of power and data lines, enabling continuous rotation in the azimuth direction. Additionally, after attaching a signal processor to the antenna module, the rotary joint commonly used in radar was no longer needed.

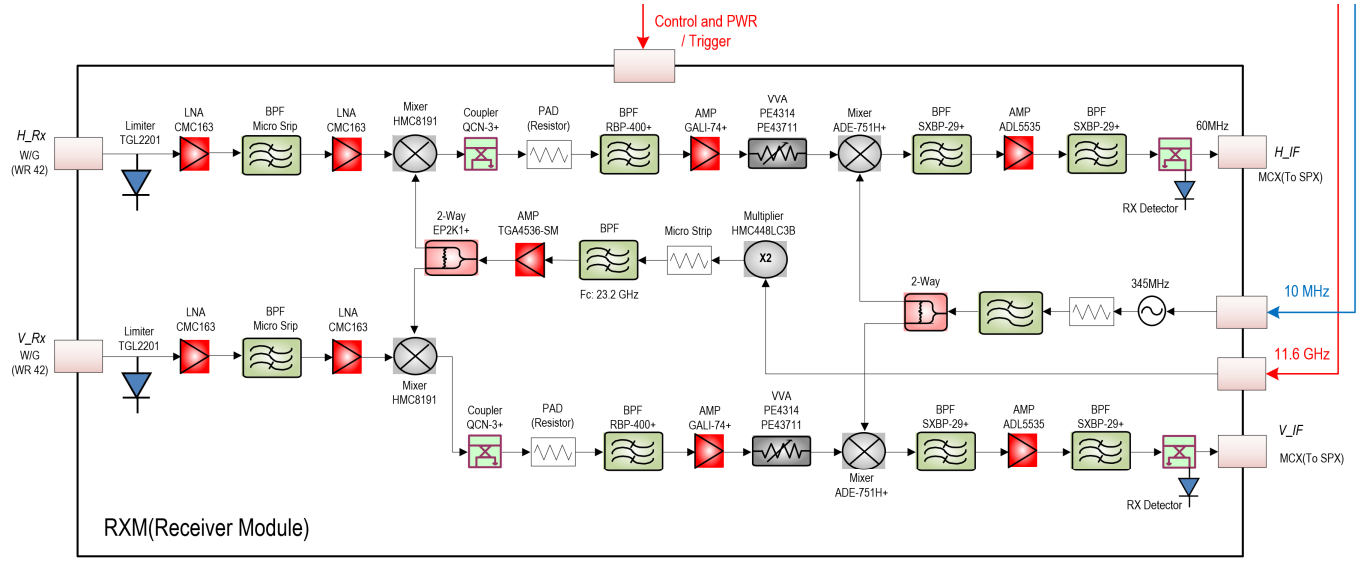

Figure 8. Block diagram of EWRG receiver.

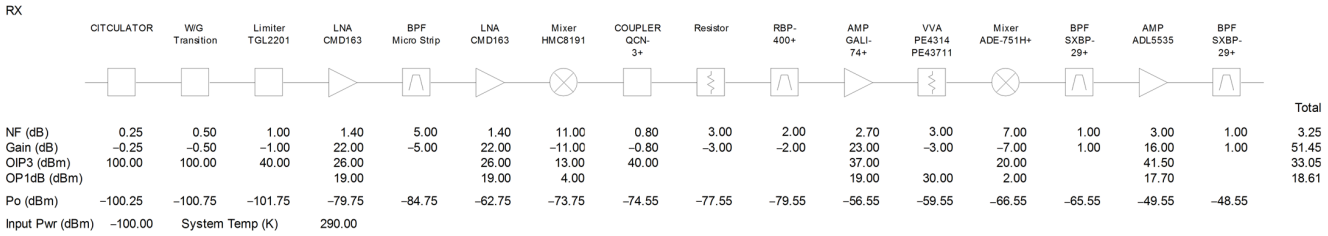

Figure 9. The power budget of the receiver.

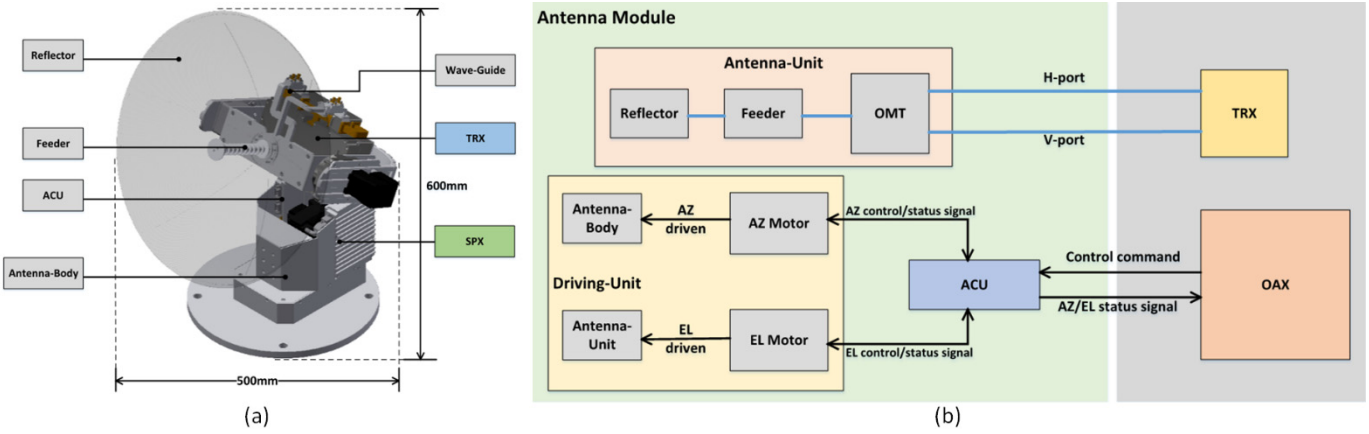

Figure 10. (**a**) The 3D design and (**b**) block diagram of the antenna module.

A radome is a protective device that shields the EWRG from external factors like humidity and temperature. It is made of Fiberglass Reinforced Plastic (FRP) material using the hand lay-up method, with a thickness of 3T (3 mm) based on the simulation of gain variation according to the radome thickness change. Additionally, at 24.15 GHz, the dielectric constant measured 3.869, and the Loss tangent (tan δ) was measured at 0.012. Figure 11 depicts the implemented antenna and the radome. An indoor radiation experiment was performed to evaluate antenna performance, and the resulting antenna beam pattern is shown in Figure 12. At a frequency of 24.15 GHz, the antenna beam width and high-level power gain for the horizontal beam are approximately 1.6° and 40.2 dBi, respectively, and for the vertical beam they are approximately 1.7° and 40.1 dBi.

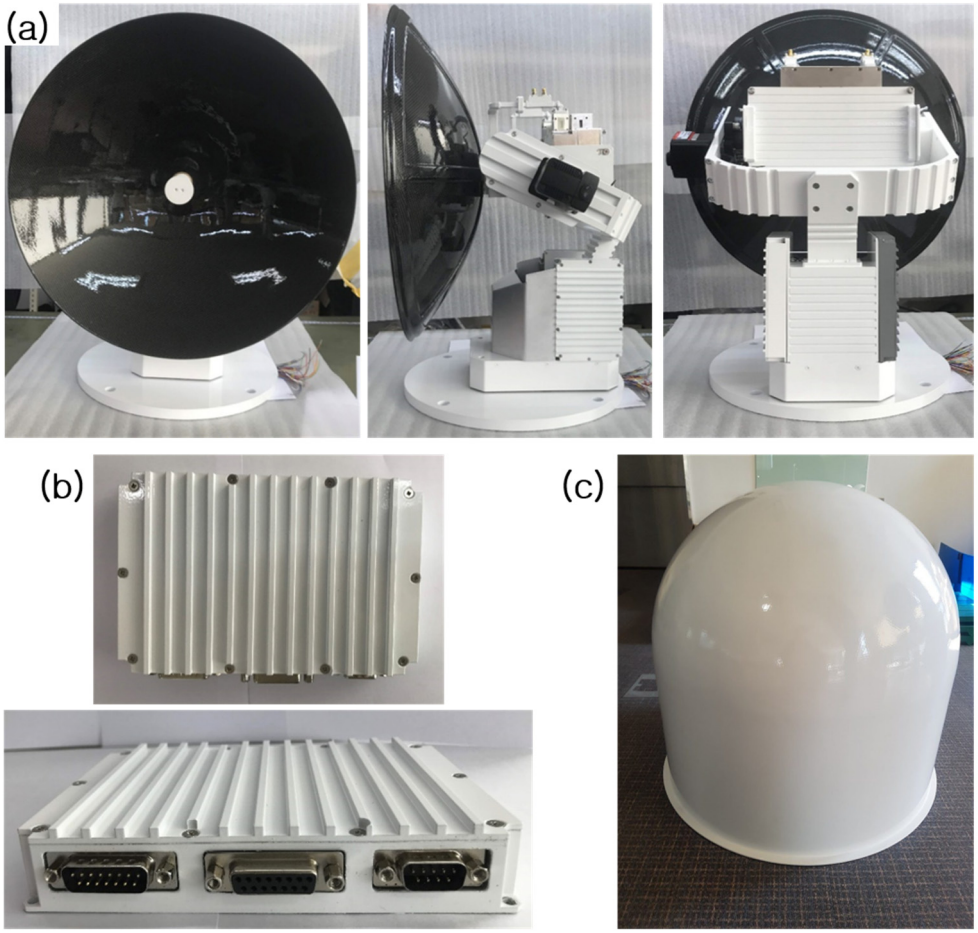

Figure 11. Implemented antenna unit (**a**) antenna, (**b**) ACU, and (**c**) radome.

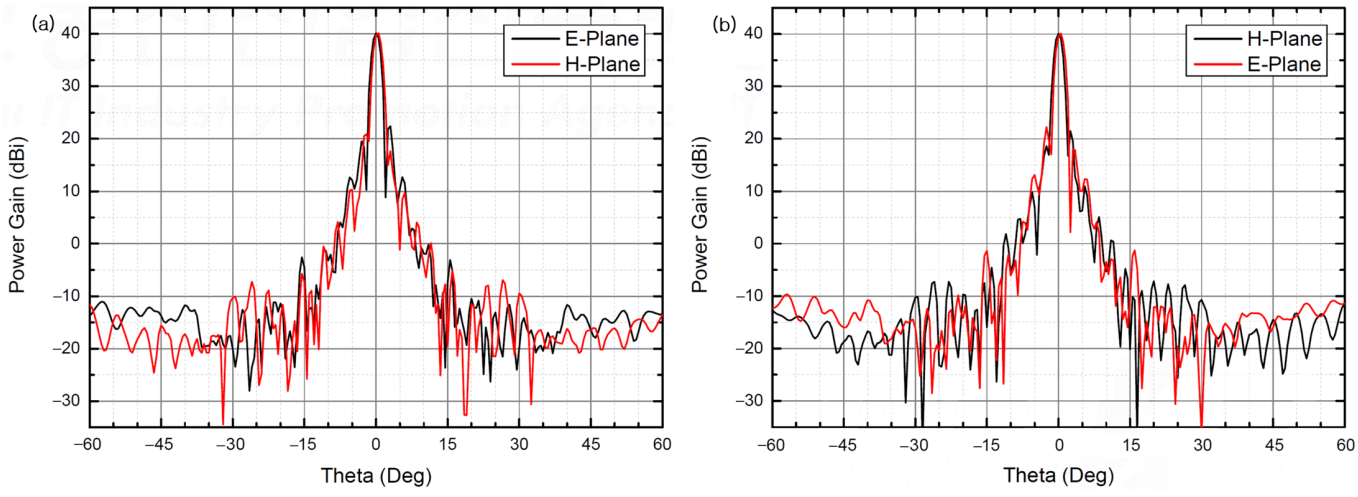

Figure 12. (**a**) Horizontal and (**b**) vertical antenna beam pattern at 24.15 GHz.

3. EWRG Signal Processor

The signal processor, through several stages of signal processing, derives correlation coefficients and meteorological parameters from the IF signal received from the transceiver, and then sends the output to the operational control server. Figure 13 depicts the EWRG signal processor.

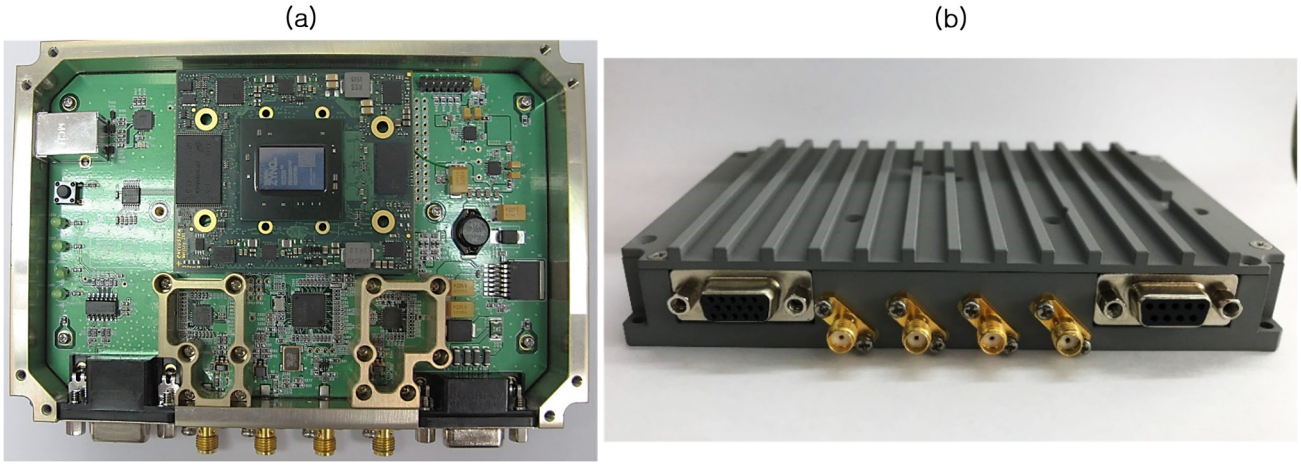

Figure 13. Implemented signal processor (**a**) internal shape, (**b**) frontal shape.

3.1. Signal Processing Procedure

The signal processor converts the H and V channel IF signals received from the transceiver into digital signals by sampling them with an ADC (Analog to Digital Converter). The digital signals are then transformed into I/Q data through DDC (Digital Down Converter) and pulse compression. Correlation coefficients and meteorological parameters are calculated from the I/Q data, and the final outputs are transmitted to the operating control server via Ethernet. Figure 14 illustrates the main signal processing procedure.

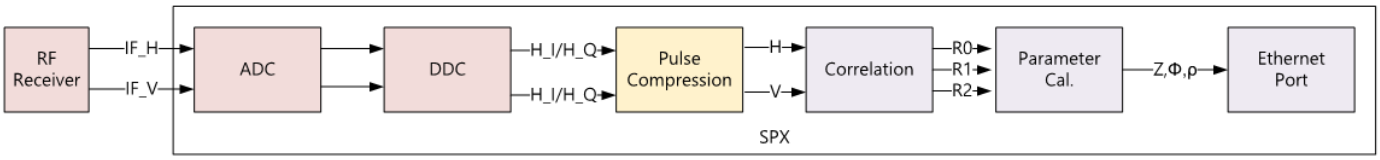

Figure 14. Signal processing procedure.

ADC sampling is performed at 16 bits and 48 MSPS for each H and V channel with a 36 MHz IF input. Since actual data acquisition occurs for 68 microseconds out of a 100-microsecond period, 3264 samples are acquired during each cycle (68 microseconds × 48 MSPS). From the 3264 sampled data, DDC generates I data by selecting samples in the sequence 1, 5, 9, 13. . . 3261 and Q data by selecting samples in the sequence 2, 6, 10, 14. . . 3262. Therefore, for each H and V channel, 816 12 MSPS data points are generated (3264/4 = 816). In the pulse compression process, a 1024-point FFT is performed on the DDC'd I/Q data, followed by multiplication with the replica, and then a 1024-point IFFT is performed. Ultimately, a pulse compression result of 32 bits and 816 samples is generated.

After pulse compressions for each cycle, correlation coefficients are calculated by gathering the results of 128 cycles. The theoretical formula for correlation coefficient calculation is as follows (Equations (3)–(6)) [21].

$$R_0 = \frac{1}{M}\sum_{n=1}^{M} \acute{s}_n^* \acute{s}_n \tag{3}$$

$$R_1 = \frac{1}{M-1}\sum_{n=1}^{M-1} \acute{s}_n^* \acute{s}_{n+1} \tag{4}$$

$$R_2 = \frac{1}{M-2}\sum_{n=1}^{M-2} \acute{s}_n^* \acute{s}_{n+2} \tag{5}$$

$$\rho_{hv}(0) = \frac{\sum s_{vv} s_{hh}^*}{\sqrt{\sum s_{vv}^2 \sum s_{hh}^2}} \tag{6}$$

The correlation coefficients R0, R1, and R2 are used to calculate single polarization meteorological variables (Reflectivity (Z), Doppler Velocity (V), and Spectrum Width (W)) for both H and V, and the dual polarization variable Differential Reflectivity (ZDR). Additionally, the dual polarization meteorological variables Correlation Coefficient (ρHV) and Differential Phase Difference (ΦDP) are derived from the cross-correlation coefficient ρhv (0). Quality control variables such as signal-to-noise ratio (SNR) and signal quality index (SQI) are also computed [22]. Meteorological variable calculation formulas are shown in Figure 15.

Z	$dBZ = 10log\left[\frac{T_0 - N}{N}\right] + dBZ_0 + 20logr + ar$	**ZDR**	$ZDR = dBZh - dBZv + ZDR_{offset}$
V	$V = \frac{\lambda}{4\pi\tau_s}\theta_1 \quad \theta_1 = arg\{R_1\} \quad \tau_s = 1/PRF$	**ρHV**	$RHOHV = \lvert\rho_{hv}(0)\rvert$
W	$W = \frac{\sqrt{Variance}}{\pi} \quad Variance = \frac{2}{3}ln\left[\frac{\lvert R_1\rvert}{\lvert R_2\rvert}\right]$	**ΦDP**	$PHIDP = arg[\rho_{hv}(0)]$
SNR	$SNR = 10log\left[\frac{R_0}{N}\right]$		
SQI	$SQI = \frac{\lvert R_1\rvert}{R_0}$		

Figure 15. Meteorological variables.

3.2. Preliminary Performance Evaluation

To verify the performance of precipitation measurement by EWRG, rainfall observations were conducted at Yeoncheon SOC Center on 09/07/18 during a period of localized heavy rainfall. The meteorological dual-polarization parameters of the EWRG were well produced, as demonstrated in Figure 16.

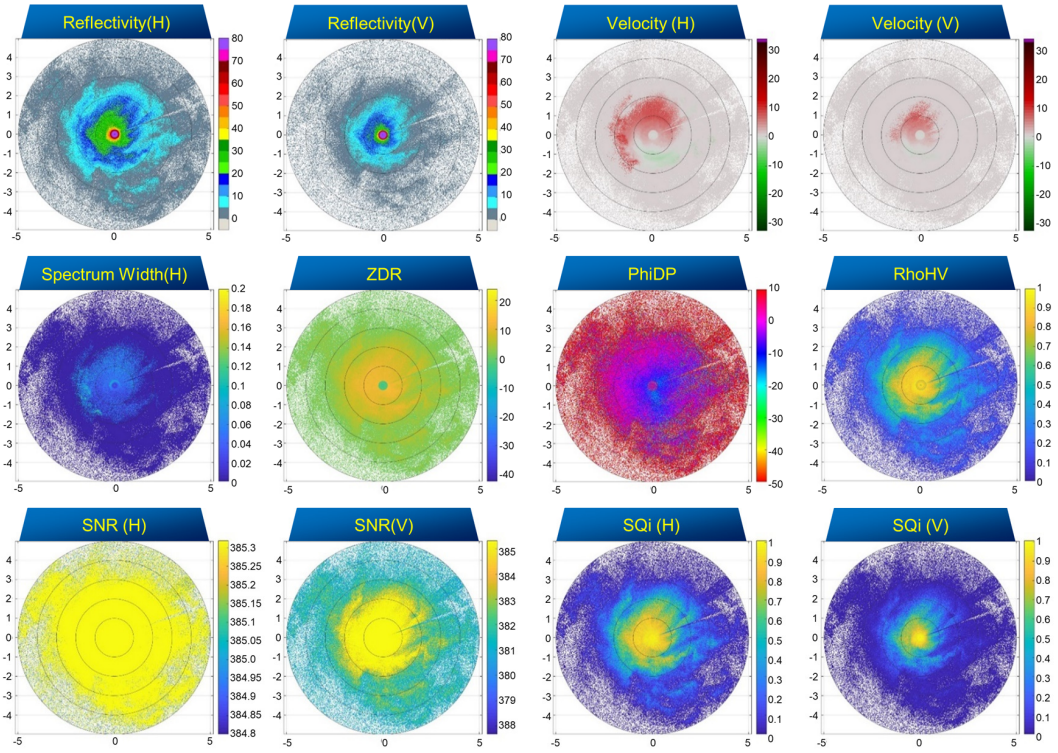

Figure 16. Rainfall observation image by EWRG (09/07/18 16:00, Yeoncheon), reflectivity at H (Z_H), reflectivity at V (Z_V), Doppler velocity at H (V_H), Doppler velocity at V (V_V), spectrum width at

H (W_H), differential reflectivity (ZDR), differential phase difference (phiDP), correlation coefficient (RhoHV), signal-to-noise ratio at H (SNR_H), signal-to-noise ratio at V (SNR_V), signal quality index at H (SQi_H), and signal quality index at V (SQi_V).

4. Summary and Conclusions

In this study, an electromagnetic wave rain gauge system for measuring precipitation using K-band dual-polarization technology was developed. The K-band EWRG is particularly effective in detecting and analyzing small-scale weather features. Additionally, the EWRG is more compact than lower frequency radar systems (S, C, and X band) and is suitable for deployment in various environments, including urban or complex mountainous areas where space might be limited.

The hardware of the EWRG combines components such as the antenna, dual-polarization RF transceiver, and FPGA signal processor. The antenna is miniaturized with a beamwidth of 2.0 degrees and a diameter of 50 cm, adopting a parabolic design. It operates in the frequency band centered at 24.125 GHz and employs simultaneous dual-polarization technology. The K-BAND pulse-driven 4 W Solid State Power Amplifiers (SSPAs) transceiver was built using small-sized Hybrid Microwave Integrated Circuit (HMIC). The transceiver consists of a power supply unit, a transmission unit, and a reception unit. It achieves an output power of over 4 W with a short duty cycle of 1% in a high-temperature environment of up to 65 degrees, and maintains a reception noise figure of 5 dB or less. The manufactured module is equipped with a waveform generation section that emits LFM and Square Pulse waveforms, while the reception unit achieves a reception gain of over 40 dB. The signal processor converts the received IF signal from the transceiver into a digital signal using an ADC. The converted digital signal then undergoes DDC and pulse compression to be transformed into I/Q data. Subsequently, from this I/Q data, final outputs such as correlation coefficients and meteorological variables are generated.

The preliminary results of the evaluation show that the meteorological parameters of the EWRG are well produced. In the future, we plan to focus on signal processing validation and improvement for dual-polarization observational variables, as well as research on the development of quantitative precipitation estimation methods.

Author Contributions: J.C. performed data analyses and conceptualization and wrote the first manuscript draft. S.L. provided helpful discussions on the analyses of data, conceptualization, and methodology, and reviewed and edited the manuscript. All authors have read and agreed to the published version of the manuscript.

Funding: This work was supported by the National Research Foundation of Korea (NRF) grant funded by the Korean government (MSIT) (No. NRF-2021R1A5A1032433) and the National Institute of Meteorological Sciences (NIMS) through Research on Weather Modification and Cloud Physics (KMA2018-00224). Additionally, research for this paper was carried out under the KICT Research Program (project no. 20220232-001, Research on Smart Construction Technology for Leading the Future Construction Industry and Creating New Market) funded by the Ministry of Science and ICT.

Data Availability Statement: Most of the data are contained within the article. Any additional data presented in this study are available upon request from the authors.

Conflicts of Interest: The authors declare no conflict of interest.

References

1. Sandsborg, J. Local rainfall variations over small, flat, cultivated areas. *Tellus* **1969**, *21*, 673–684. [CrossRef]
2. Jackson, I.J. Tropical rainfall variations over a small area. *J. Hydrol.* **1969**, *8*, 99–110. [CrossRef]
3. Sevruk, B. Adjustment of tipping-bucket precipitation gauge. *Atmos. Res.* **1996**, *42*, 237–246. [CrossRef]
4. Groisman, P.Y.; Legates, D.R. The accuracy of United States precipitation data. *Bull. Am. Meteorol. Soc.* **1994**, *75*, 215–227. [CrossRef]
5. Soren, T. Weather Radar Rainfall Data in Urban Hydrology. *Hydrol. Earth Syst. Sci.* **2017**, *21*, 1359–1380.
6. Hunter, S.M. WSR-88D Radar rainfall estimation: Capabilities, limitations and potential improvements. *Natl. Weather Dig.* **1996**, *20*, 26–36.

7. Jang, B.J.; Kim, W.; Lim, S.; Choi, J.H. Analysis of Rainfall Cases and Their Observed Signal from Prototype of Electromagnetic Wave Rain Gauge. *Inst. Electron. Inf. Eng. Conf.* **2018**, *41*, 492–493.
8. Peters, G.; Fischer, B.; Andersson, T. Rain observations with a vertically looking Micro Rain Radar (MRR). *Boreal Environ. Res.* **2002**, *7*, 353–362.
9. Choi, J.H.; Lee, B.K.; Park, H.S.; Park, J.M.; Lim, S. Design of FPGA-based Signal Processing of EWRG for Localized Heavy Rainfall Observation. *J. Korea Inst. Inf. Commun. Eng.* **2020**, *24*, 1215–1223.
10. Chong, M.K.; Na, H.G. A Development of the X-Band 63 Watt Pulsed SSPA for Radar. *J. Electromagn. Eng. Sci.* **2011**, *22*, 380–388.
11. Frank, G. Status and Future Strategy for Advanced High Power Microwave Sources for Accelerators. In Proceedings of the 9th International Particle Accelerator Conference, Vancouver, BC, Canada, 29 April–4 May 2018.
12. Kang, D.M.; Min, B.G.; Lee, J.M.; Yoon, H.S.; Kim, S.I.; Ahn, H.K.; Kim, D.Y.; Kim, H.C.; Lim, J.W.; Nam, E.S. 0.25 μm AlGaN/GaN HEMT Devices and 9 GHz Power Amplifier. *J. Electromagn. Eng. Sci.* **2016**, *27*, 76–79. [CrossRef]
13. Kwon, G.W.; Koh, J.H. Modified LFM Signal in Radar Application. In Proceedings of the KICS Summer Conference, Jeju, Korea, 19–21 June 2013; pp. 762–763.
14. Yoon, J.H.; Yoo, S.O.; Lee, D.J.; Ye, S.H. LFM Radar Implemented in SDR Architecture. *J. Electromagn. Eng. Sci.* **2018**, *29*, 308–315. [CrossRef]
15. Ha, C.H.; Kwon, B.J.; Lee, M.G. Radar Signal Processor Design Using FPGA. *J. KIMS Technol.* **2017**, *20*, 482–490.
16. Richards, M.A.; Scheer, J.A.; Holm, W.A. *Principles of Modern Radar: Basic Principles*; SciTech Publishing: Edition, NJ, USA, 2010.
17. Rawat, C.D.; Sarate, A.D. High resolution low power radar pulse compression techniques. *Int. J. Adv. Res. Electr. Electron. Instrum. Eng.* **2014**, *3*, 8928–8935.
18. Kumar, A.; Nidhi. Radar pulse compression technique for linear frequency modulated pulses. *Int. J. Eng. Tech. Res.* **2015**, *3*, 33–35.
19. Tsukamoto, N.; Yamauchi, H.; Okumura, H.; Umehara, A.; Kajiwara, Y. JMA's C-band dual-polarization Doppler weather radars with SSPAs. In Proceedings of the WMO Technical Conference on Meteorological and Environmental Instruments and Methods of Observation 2016, Madrid, Spain, 27–30 September 2016.
20. Choi, J.H.; Lim, S.H.; Park, H.S.; Lee, B.K. Design and Implementation K-Band EWRG Transceiver for High-Resolution Rainfall Observation. *J. Korea Inst. Inf. Commun. Eng.* **2020**, *24*, 646–654.
21. Doviak, R.; Zrnic, D.S. *Doppler Radar and Weather Observations*, 2nd ed.; Academic Press: San Diego, CA, USA, 1993.
22. Choi, J.; Yoo, C.; Lim, S.; Han, M.; Lee, B. Quality Control Algorithm of Rainfall Radar Image for Uncertainty of Rainfall. *J. Korea Multimed. Soc.* **2017**, *21*, 1874–1889.